Article

Bioinspired Water Oxidation using a Mn-Oxo Cluster Stabilized by Non-Innocent Organic Tyrosine Y161 and Plastoquinone Mimics

Joaquín Soriano-López, Rory Elliott, Amal C Kathalikkattil, Ayuk M. Ako, Muhamed Mulahmetovi#, Munuswamy Venkatesan, and Wolfgang Schmitt

ACS Sustainable Chem. Eng., **Just Accepted Manuscript** • DOI: 10.1021/acssuschemeng.0c03379 • Publication Date (Web): 17 Aug 2020

Bioinspired Water Oxidation using a Mn-Oxo Cluster Stabilized by Non-Innocent Organic Tyrosine Y161 and Plastoquinone Mimics

Joaquín Soriano-López[1*], Rory Elliott[1], Amal C. Kathalikkattil[1†], Ayuk M. Ako[1§], Muhamed Mulahmetović[1], Munuswamy Venkatesan[2], and Wolfgang Schmitt[1*].

[1] School of Chemistry & SFI AMBER Centre, Trinity College, University of Dublin, Ireland.
[2] School of Physics & CRANN Institute, Trinity College, University of Dublin, Ireland.

*Correspondence to: schmittw@tcd.ie,
sorianoj@tcd.ie

Joaquín Soriano-López: sorianoj@tcd.ie
Rory Elliott: relliot@tcd.ie
Amal C. Kathalikkattil: amalcherian@gmail.com
Ayuk M. Ako: akomana12@gmail.com
Muhamed Mulahmetović: mulahmem@tcd.ie
Munuswamy Venkatesan: venkatem@tcd.ie
Wolfgang Schmitt: schmittw@tcd.ie

ABSTRACT: The complexity and energy demand of the H_2O oxidation half-reaction represents the bottleneck for the development of sustainable, environmentally friendly H_2 economies using H_2O as energy feedstock. In Nature, photosynthetic H_2O oxidation processes occur in photosystem-II (PS-II) and are facilitated by the Oxygen Evolving Complex (OEC), a manganese-oxo cluster $\{Mn_4CaO_5\}$ with cubane-like topology. In recent years, the use of manganese-based H_2O oxidation catalysts has attracted significant scientific attention, not only to mimic and understand naturally occurring processes, but also due to the low toxicity and high abundancy of Mn in the Earth's crust. Here we report the catalytic H_2O oxidation activity at pH 7.2 of a high-nuclearity manganese-oxo cluster. The species, which contains multiple cubane motifs and which is stabilized by redox-active aromatic organic ligands, gives rise to an onset overpotential as low as 255 mV when dispersed in a carbon paste matrix, achieving high current densities of 10 mA cm^{-2} and even 100 mA cm^{-2} at η = 482 and 654 mV, respectively. The electrodes show good stability under turnover conditions for 7 hrs. Additionally, direct light-induced O_2 evolution measurements confirm a reaction rate of 0.72 s^{-1} and turnover number (TON) of up to 55. The outlined experimental concept demonstrates how a synergistic effect between non-innocent, redox-active organic ligands and bio-inspired Mn oxo-clusters resembling the natural $\{Mn_4CaO_5\}$ unit, that are dispersed in a conductive carbon matrix and protected by a Nafion membrane, can facilitate remarkably high catalytic activity under neutral, environmentally friendly pH conditions.

KEYWORDS: Oxygen Evolution Reaction; Manganese; Redox-active Ligand; Heterogeneous Electrocatalysis

INTRODUCTION

Growing global energy demands to reach the projected 70 terawatts requirement by 2050 and rinsing atmospheric CO_2 levels impose imperatives for the development of sustainable, carbon-neutral energy concepts.[1–3] Owing to its natural abundance, water represents the ideal source of reducing equivalents to generate H_2, thus storing energy in chemical bonds and providing a non-carbon fuel with high gravimetric energy density.[4] However, technological breakthroughs are hampered by the lack of cost-effective catalysts for the highly endergonic 4-electron H_2O oxidation half-reaction (Eq. 1) of the overall water splitting process, also known as the oxygen evolution reaction (OER).[5–7] The complexity and energy demand of this reaction are illustrated by large overpotentials (η) associated with the individual reaction steps.[8] To date, noble metal oxides or related molecular Ru or Ir complexes are promising catalysts that highlight conceptual pathways to viable systems with satisfactory O_2 conversion rates.[9,10] However, scarcity and prohibitive costs prevent their large-scale application. In recent years, catalysts containing earth-abundant metal ions are emerging.[11–13] Noteworthy are molecular species, containing Co^{II}, Cu^{II} and Fe^{II} ions,[14–16] colloidal particles and homo- and heterometallic oxides.[17–21]

$$2H_2O_{(l)} \rightarrow O_{2(g)} + 4H^+ + 4e^- \qquad E^\circ = 1.23 \text{ V vs RHE}$$
(Eq. 1)

Environmental and economic concerns arise from the currently applied industrial electrolyzers that operate, either in strongly acidic or basic media, in which charge-carrier

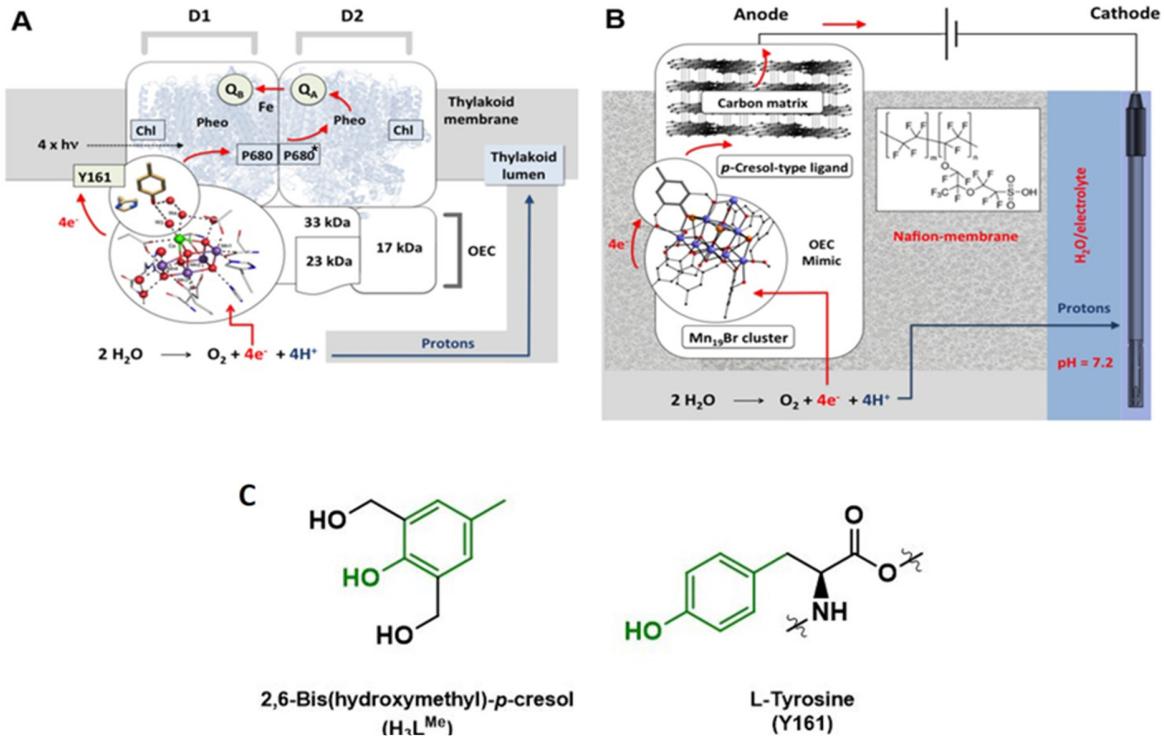

Figure 1. Water oxidation catalysis and electron transport. (A) Schematic representation of the water oxidation process in green plants in photosystem-II (PS-II); D1, D2 are the protein subunits that form the core of the PS-II. These two proteins contain different cofactors among which are electron acceptor quinones (Q_A, Q_B), the chlorophyll special pair P680, pheophytin (Pheo), non-haem iron (Fe), and the Oxygen Evolving Center (OEC), in which the $\{Mn_4CaO_5\}$ cluster and the tyrosine Y161 are highlighted. (B) Schematic representation of the applied electrocatalytic water oxidation setup using a Mn-oxo cluster and electron-mediating ligands in **Mn_{19}Br**, dispersed in a conductive carbon matrix and using a Nafion membrane as a proton conductor. (C) Comparison of the organic moieties present within **Mn_{19}Br** and the OEC. Structures of the redox-active *p*-cresol ligand H_3L^{Me} which stabilizes **Mn_{19}Br**, and the tyrosine residue that oxidizes the $\{Mn_4CaO_5\}$ cluster of the OEC in PS-II. Analogous structural elements are highlighted green.

transfers proceed at optimum performance.[22] This operational boundary impedes the use of photoanodes for *direct* 'solar-to-fuel' technologies as light-absorbing semiconductors suffer from fast degradation under such extreme conditions. Hence, external photovoltaic (PV) cells are used in *indirect* processes in combination with external electrolyzers whereby light is initially harvested, stored and then converted into fuel in consecutive steps.[23] In addition to high investment costs and environmental considerations, the efficiencies of such two-step approaches are limited to *ca.* 60 % due to input energy losses. Catalysts that perform under mild conditions at neutral pH values circumvent these intrinsic drawbacks,[24] can *directly* be used in photoelectrocatalytic (PEC) devices and are conceptionally employable to electrolyze raw seawater at offshore plants.[25] Significant advances have recently been reported on the use of electrocatalysts that are composed of earth-abundant metal ions and that operate at neutral pH conditions.[26–30] However, improvements are required to achieve satisfactory current densities of 10 mA cm^{-2}.[31–33] at low overpotentials to target direct solar-to-fuel conversion efficiencies of 10 %.[5,34,35] Particularly, the discovery of OER catalysts composed of non-toxic earth-abundant elements that meet such benchmark characteristics, as outlined by Symes and co-workers,[13] are expected provide a breakthrough for the advancement of new artificial photosynthetic systems.

Nature uses a $\{Mn_4CaO_5\}$ oxo-cluster in the oxygen evolving complex (OEC) to oxidize water at close-to-neutral pH values. Spectroscopic and computational studies have yielded new mechanistic insights into the naturally occurring OER.[36,37] Active bio-inspired catalysts should be compatible with Kok redox cycle and the proposed acid-base (AB) or direct coupling (DC) mechanisms,[7] and enable multiple electron transfers (ET) or proton-coupled processes (PCET) within a narrow potential range[38]. Under this purview, Mn-oxo clusters featuring cores containing cubane motifs resembling the $\{Mn_4CaO_5\}$ cluster of the OEC and non-innocent organic ligands are highly appealing and have not yet satisfactorily been explored for catalytic purposes. These clusters can accumulate multiple charge equivalents in a single molecule, thus facilitating demanding multiple-electron redox processes. In addition, the high abundance of Mn in the Earth's crust (12th largest),[39] its availability[†] and low toxicity, make Mn-based OER catalysts highly attractive. However, Mn-oxo clusters typically suffer from stability issues under harsh OER

conditions, resulting either in the *in-situ* formation of active, catalytically persisting, heterogeneous manganese oxides (MnO_x),[40] or fast catalytic decay due to catalyst deactivation.[41] Examples of previously investigated synthetic Mn catalysts include cubane-like $\{Mn_4O_4\}$ diarylphosphinates,[42] an acetate-stabilized tetramanganese polyoxometalate (onset overpotential of 530 mV at pH = 5.2)[43] and a Mn-based Weakley-type polyoxometalate OER electrocatalyst that operates at neutral pH.[41] Amongst the most interesting Mn-oxo clusters, are dodecanuclear $[Mn_{12}O_{12}(OAc)_{16-x}L_x(H_2O)_4]$ complexes (L = acetate, benzoate, benzenesulfonate, diphenylphosphonate or dichloroacetate)[44] that display onset overpotentials varying between 640 and 820 mV (at 0.2 mA cm^{-2}) under heterogeneous conditions, whilst the introduction of di- or trihydroxybenzoate ligands increases the solubility of the $\{Mn_{12}\}$ derivatives leading to high catalytic OER performance that is observed at pH = 6 in homogeneous solutions.[45,46]

Indeed, the limited stability exhibited by Mn-oxo clusters is not surprising, considering that the OEC and its surroundings also constantly undergo degradation during O_2 evolution; however, self-repair mechanisms re-constitute the OEC's integrity, without which its activity would cease within 30 minutes.[47] It is notable that the efficacy of the biological enzymatic systems in green plants is determined by effective charge separation and electron mobility mechanisms (Figure 1A).[48] Initial chlorophyll-based photoexcitation causes charge separation involving the oxidation of P680 to a radical cation $P680^{\bullet+}$ and the reduction of a pheophytin molecule. Subsequent electron transfer processes facilitate plastoquinone reduction to plastoquinole. Water constitutes the ultimate source of the electrons that are abstracted by the $\{Mn_4CaO_5\}$ cluster and are directly transferred to a tyrosine residue Y161 of the D1 peptide. The 4-methylene phenol moiety of the latter tyrosine amino acid can be considered as a cresol derivative and provides an oxidizable side-chain. It locates directly at the periphery of the $\{Mn_4CaO_5\}$ cluster and is responsible for the recovery of the P680 ground state through rapid electron injection. Whilst the photoexcitation process is a one-photon/one-electron process, plastoquinone reduction and water oxidation are two- and four-electron processes, respectively. Hence, these chemical transformations require charge accumulation coupled to protonation reactions involving intermediates that are stabilized by the protein environment.

Here we report the electrocatalytic OER activity of a bio-inspired, high-nuclearity Mn-oxo cluster, $[Mn^{III}_{12}Mn^{II}_7(\mu_4\text{-}O)_8(\mu_3\text{-}OCH_3)_2(\mu_3\text{-}Br)_6(HL^{Me})_{12}(MeOH)_5(MeCN)]Br_2{\cdot}9MeCN{\cdot}MeOH$ (**Mn_{19}Br**), which can facilitate high catalytic OER performance characteristics under neutral pH conditions. As part of a modified carbon paste electrode, **Mn_{19}Br** displays an onset overpotential as low as 255 mV and achieves high current densities of 10 mA cm^{-2} and even 100 mA cm^{-2} at applied overpotentials of 482 and 654 mV at pH = 7.2, respectively. Direct O_2 evolution measurements under light-induced OER conditions corroborates the catalytic activity. Post-catalytic characterizations identify the **Mn_{19}Br** complex as the true catalyst, whereby no other active species could be detected. The **Mn_{19}Br** system reveals remarkable OER activity at pH ≈ 7, whereby the combination of achievable current densities, onset overpotentials and good turnover characteristics stems from a synergistic effect between non-innocent, redox-active organic ligands and multiple Mn sites that are dispersed in a conductive carbon-based matrix which is separated from the bulk water electrolyte using a Nafion membrane that acts as a proton shuttle. The applied approach adopts some key-principles of the co-factor of PS-II and highlights a new conceptional avenue for the development of effective catalysts for direct 'solar-to-fuel' energy conversion technologies using benign, abundant cluster-based compounds which are stabilized by bio-relevant oxidizable organic ligands that mimic the natural tyrosine Y161 or plastoquinone functionalities.

RESULTS

The Structure of Mn_{19}Br. Mixed-valent, polynuclear Mn complexes in which the transition metal ions are organized to form supertetrahedral structures establish rational synthetic avenues to species with multiple $\{Mn_4O_4\}$ cubane motifs. Their underlying synthetic approaches, and a judicious choice of stabilizing redox-active ligands enable the preparation of polynuclear Mn complexes that potentially mimic both the Mn core structure of the OEC and its surrounding organic tyrosine Y161 mediator or plastoquinone environment. Hence, such oxo-clusters can facilitate the establishment of new electrochemical systems that replicate key features of the natural enzymes (Figure 1B).

The use of the tridentate 2,6-bis(hydroxymethyl)-*p*-cresol ligand (H_3L^{Me}) (Figure 1C) in the presence of $MnBr_2$ in an acetonitrile/methanol mixture results in the formation of a variant of Mn cluster with supertetrahedral core structure, $[Mn^{III}_{12}Mn^{II}_7(\mu_4\text{-}O)_8(\mu_3\text{-}OCH_3)_2(\mu_3\text{-}Br)_6(HL^{Me})_{12}(MeOH)_5(MeCN)]Br_2{\cdot}9MeCN{\cdot}MeOH$ (**Mn_{19}Br**). $\{Mn_{19}\}$ coordination clusters with supertetrahedral core structures were previously reported by Powell coworkers, revealing ferromagnetic interactions between the spin centers and leading to a maximum-spin ground state of $S = 83/2$.[49,50] Noteworthy, the use of **Mn_{19}Br** as catalysts for the oxidation of benzyl alcohol to benzaldehyde was recently reported.[51]

The compound reproducibly forms phase-pure in good yields. Single-crystal X-ray analyses (Table S1) confirmed that it consists of a molecular, nonadecanuclear $\{Mn_{19}\}$ species and can be regarded as a dimer of two supertetrahedral $\{Mn^{III}_6Mn^{II}_4\}$ units sharing a common Mn^{II} vertex. The $\{Mn^{III}_6Mn^{II}_4\}$ unit is composed of a central $\{Mn^{III}_6\}$ assembly with octahedral atom arrangement (Figure 2). Four of the 8 triangular faces of the octahedron are stabilized by μ_3-Br^- or μ_3-OMe^- ligands; the remaining faces are capped by μ_4-O^{2-} oxo ligands that connect the inner $\{Mn^{III}_6\}$ unit to four outer Mn^{II} atoms that adopt a tetrahedral $\{Mn^{II}_4\}$ topology. In contrast to the 6-coordinate Mn^{II} ion that connects the two supertetrahedra, each of the peripheral 7-coordinate Mn^{II} ions is coordinated by a MeOH or MeCN solvent molecule. The $\{Mn_{19}\}$ cation is stabilized by 12 partially deprotonated organic $(HL^{Me})^{2-}$ ligands, whereby one

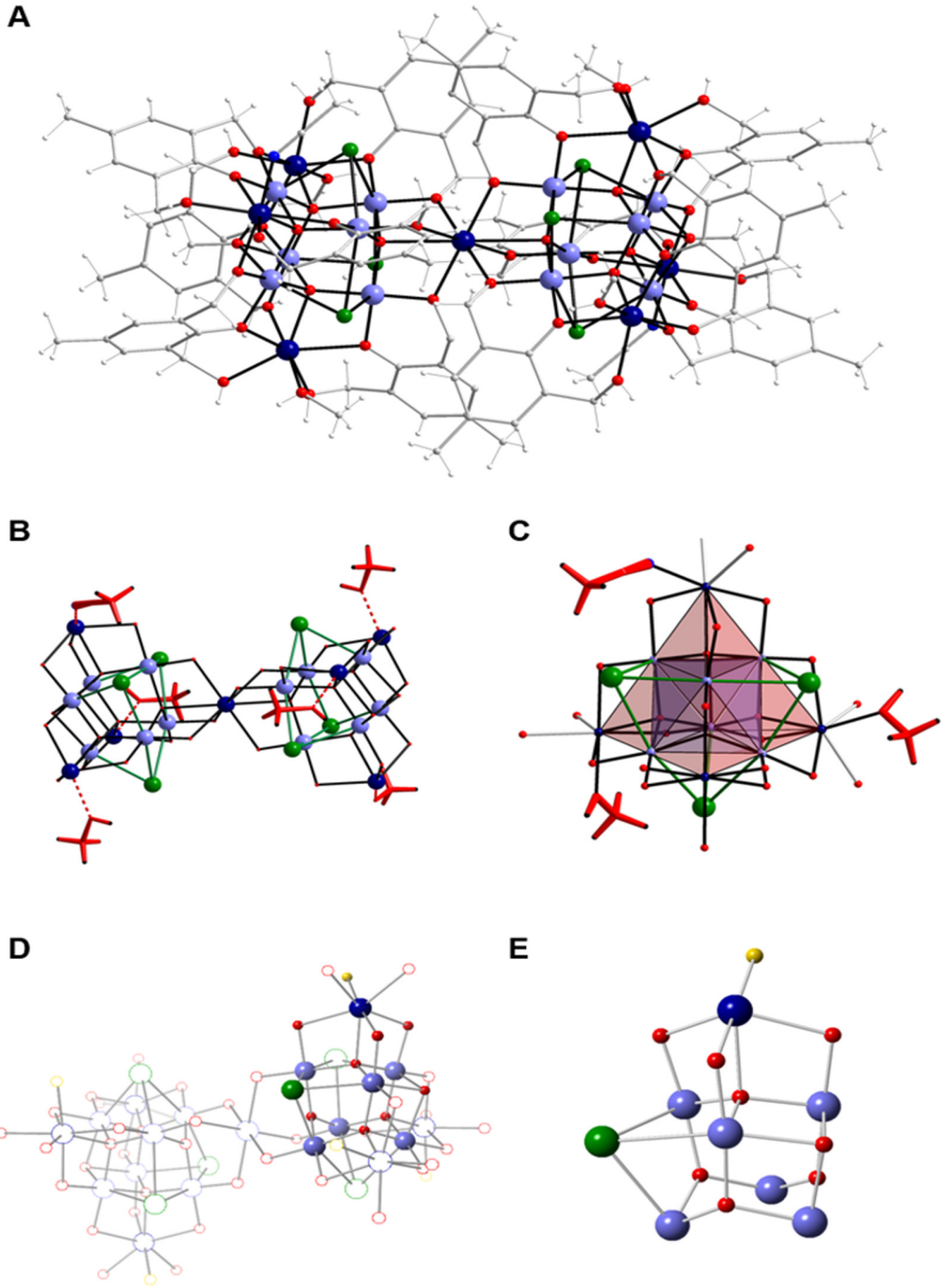

Figure 2 Single crystal X-ray structure of **$Mn_{19}Br$.** (A) Molecular structure of $[Mn^{III}_{12}Mn^{II}_{7}(\mu_4\text{-}O)_8(\mu_3\text{-}OCH_3)_2(\mu_3\text{-}Br)_6(HL^{Me})_{12}(MeOH)_5(MeCN)]^{2+}$; (B) Core structure of **$Mn_{19}Br$** in which the organic ligands have been omitted for clarity. (C) $\{Mn^{III}_6Mn^{II}_4\}$ supertetrahedral core in **$Mn_{19}Br$**. The labile solvent ligands that bind to the active Mn^{II} centers are highlighted as red wireframe representation. (D) and (E) Cubane-type arrangements in the $\{Mn^{III}_6Mn^{II}_4\}$ core of **$Mn_{19}Br$**. Color code: Mn^{II} (dark blue), Mn^{III} (pale blue), Br (green), C (grey), O (red), N (blue), H (white/grey); solvent position in D and E are shown as yellow spheres.

methyl alcohol moiety remains protonated while the second methyl alcohol and the phenolic hydroxyl functions are deprotonated. The constitutional formula of **$Mn_{19}Br$** and the assignment of the oxidation states are unambiguous and in agreement with bond valence sum analyses, observed geometrical parameters and charge balance considerations. The assignment further agrees with the temperature-dependent magnetic susceptibility measurements by which ferromagnetic interactions between 12 high-spin Mn^{III} ($S = 5/2$) and 7 high-spin Mn^{II} ($S = 2$) ions impart the max. possible spin ground state of $S = 83/2$ (Figure S1).[49,50] Moreover, a cyclic voltammogram of a 1 mM

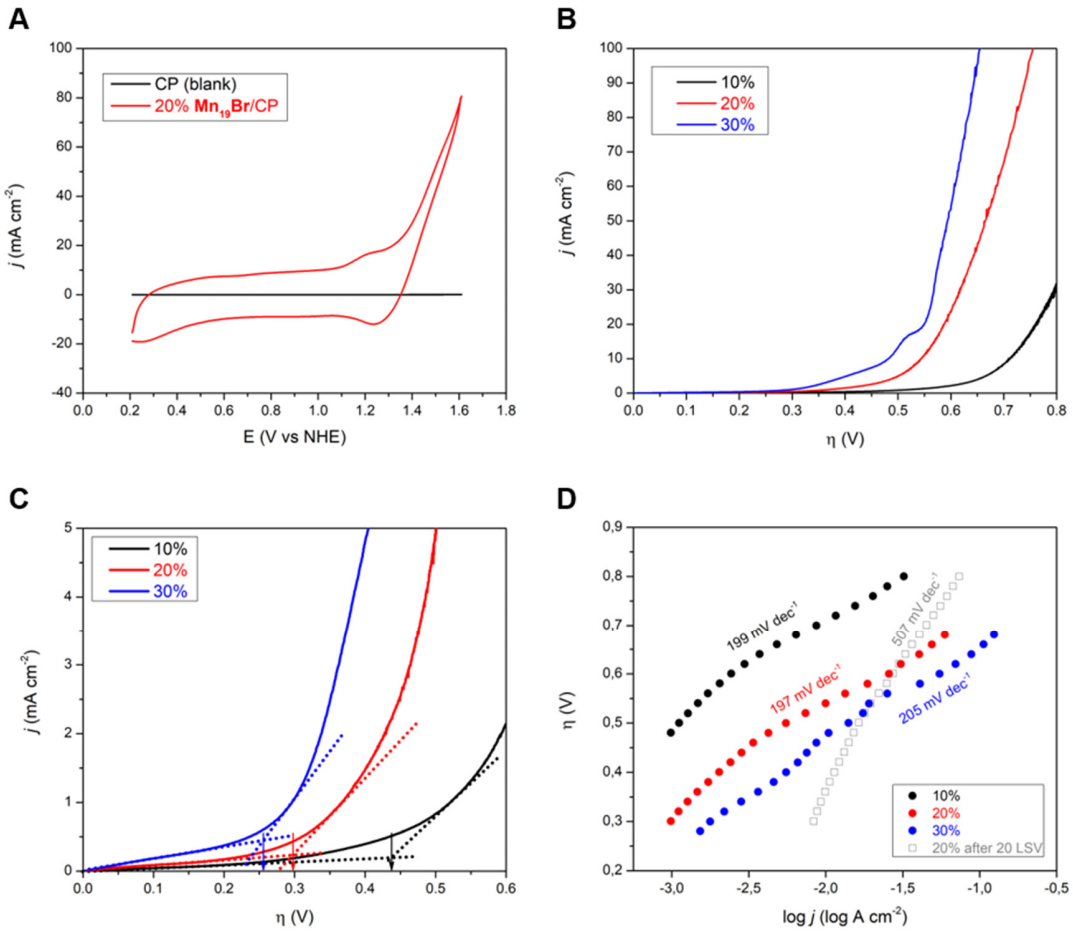

Figure 3. Electrocatalytic OER activity of **$Mn_{19}Br$**. (A) Cyclic voltammogram of a 20 wt.-% **$Mn_{19}Br$**/CP blend working electrode (red) compared to a carbon-paste-only (CP) electrode (black). (B) Linear sweep voltammetry using **$Mn_{19}Br$**/CP electrodes at various catalyst loadings. (C) Calculation of the onset potential from linear sweep voltammetry. The arrows indicate the onset of electrocatalytic water oxidation. (D) Plots of η *vs*. log *j* obtained from **$Mn_{19}Br$**/CP electrodes at different catalyst loadings. Grey open circles highlight the Tafel plot obtained after catalyst deactivation.

solution of **$Mn_{19}Br$** in DMF reproduces the previously reported electrochemical response, showing the irreversible oxidation of the seven Mn^{II} atoms to Mn^{III} at 0.75 V vs SCE (Figure S2).[51]

A closer examination of the **$Mn_{19}Br$** core topology reveals some resemblance to the $\{Mn_4CaO_5\}$ cluster in the OEC. The reactive site of **$Mn_{19}Br$** can be regarded as a $\{Mn_7BrO_8\}$ cluster in which two cubane structures are fused and the 'dangling', peripheral, partially-solvated Mn^{II} atoms may act as the catalytically active centers (Figure 2). It is further noteworthy that the presence of the Br atoms in the **$Mn_{19}Br$** structure is not negligible. Akin to the larger Ca^{2+} ion in the $\{Mn_4CaO_5\}$ cluster, the Br^- anion imposes distortion to the $\{Mn_7BrO_8\}$ unit. Such structural effects are often considered to play a pivotal role for high OEC activity;[52] here, a possible participation of the halide centers within a catalytic reaction mechanism cannot be discarded.

Electrocatalytic OER Activity. The structural attributes of the **$Mn_{19}Br$** species, in which six partially solvated Mn-atoms facilitate binding sites for water substrates and in which closely-located μ-O-bridged Mn atoms provide direct electronic pathways to distribute oxidation equivalents, prompted us to evaluate its electrocatalytic OER activity. Importantly, the electronic features of the *p*-cresol $(HL^{Me})^{2-}$ ligand derivatives were expected to aid the abstraction of electrons from water similarly to Y161, resulting in the formation of quinone derivatives and thus leading to higher catalytic activity.[53] Further, the hydrophobic nature of the $(HL^{Me})^{2-}$ ligands provides a dielectric environment that prevents the dissolution of the Mn-oxo cluster in water at room temperature (average particle size of ca. 310 nm, see DLS experiments in Figure S3), thus allowing advantageous, defined electrocatalytic studies in the solid state. Heterogeneous electrocatalytic OER activity experiments were conducted using commercial carbon paste (CP) as a conductive matrix. For this purpose, **$Mn_{19}Br$** was blended with CP at different weight ratios (wt.-%), to produce **$Mn_{19}Br$**-modified carbon paste electrodes (**$Mn_{19}Br$**/CP) which were used as working electrodes.[54] In an attempt to replicate the mild, aqueous operation

conditions of PS-II, the experiments were conducted in aqueous phosphate buffer at pH 7.2 using KNO_3 (1 M) as electrolyte.

Initially performed cyclic voltammetry (CV) experiments employing a 20 wt.-% **$Mn_{19}Br$**/CP electrode resulted in significantly increasing current densities which contrasts with the electrochemical behavior of pure CP electrodes (control experiment) and clearly demonstrates **$Mn_{19}Br$**-derived catalytic OER activity (Figure 3A). Following, the catalyst content within the carbon blends was varied and optimized using linear sweep voltammetry (LSV) experiments. The **$Mn_{19}Br$** loading within the CP blend was limited to 30 wt.-% as higher relative quantities resulted in brittle materials that were mechanically difficult to handle. The LSV responses from **$Mn_{19}Br$**/CP electrodes with 10, 20, and 30 wt.-% catalyst content are shown in Figure 3B. Generally, increasing **$Mn_{19}Br$** quantities in the CP blend results in higher catalytic OER activity, hence 30 wt.-% **$Mn_{19}Br$**/CP electrodes exhibit the best performance, reaching 10 mA cm^{-2} at η = 482 mV and even 100 mA cm^{-2} at η = 654 mV (Table 1). Moreover, the 30 wt.-% **$Mn_{19}Br$**/CP electrodes display a remarkably low onset overpotential of only 255 mV under working conditions at pH = 7.2 (Figure 3C).

The origin of these, cumulatively, high activity characteristics warranted a more detailed analysis. In agreement with other electrochemical studies using biomimetic cubane-type Mn clusters and other Mn^{II} compounds, the **$Mn_{19}Br$**/CP electrode shows an irreversible redox process centered at 1.22 V vs NHE which was previously attributed to the irreversible oxidation of the seven Mn^{II} atoms to Mn^{III} of the **$Mn_{19}Br$** cluster.[51] Interatomic distances within the cluster are expected to vary upon oxidation as the electronic structure of the oxo-cluster changes. Nevertheless, we could not observe such structural transitions during the post-catalytic characterization experiments, most probably as Mn^{II} ions are recovered during the catalytic cycle after O_2 release upon water displacement.

Particularly characteristic in the **$Mn_{19}Br$**/CP system are crossover loop processes that take place during the first 3 CV cycles and which result in significantly higher current densities and increased catalytic activity (Figure S4). This electrochemical behavior derives from the redox activity of the $(HL^{Me})^{2-}$ ligands of the **$Mn_{19}Br$** cluster, as demonstrated by CV experiments using the Mn-free H_3L^{Me}/CP electrodes (Figure S5). Under these conditions, the organic *p*-cresol type ligand undergoes oxidation to form a semihydroquinone, semiquinone or carboxylate derivatives.[55] Interestingly, the crossover behavior is only observed when dispersed in a CP matrix, suggesting that the resulting radical species interact with this carbon material. Thus, the data clearly underlines that the organic ligand promotes electron transport between the Mn cluster core and the stabilizing carbon matrix, and its function is comparable to the role of the redox mediators that provide electron transport pathways within the protein environment of PS-II.

Kinetic Data and Bulk Water Electrolysis. The kinetics of different **$Mn_{19}Br$**/CP blends were studied using Tafel plots, which were derived from the LSV data (Figure 3D). The three different electrodes yield consistent slopes varying closely between 197 and 205 mV dec^{-1}. The slope exclusively depends on the rate-determining step of an electrochemical process. The data is consistent with the features observed during the CV experiments. The obtained values, which are higher than the typical Tafel slopes (≤120 mV dec^{-1}), suggest that the kinetics of the catalytic OER is limited by a diffusion process and electron transfer within the **$Mn_{19}Br$**/CP electrodes.[56]

Table 1. Comparison of the linear sweep voltammetry data obtained using $Mn_{19}Br$/CP working electrodes containing different catalyst loadings.

wt.-% **$Mn_{19}Br$**/CP	10	20	30
η_{onset} (mV)	438	297	255
η (mV) @ j = 1 mA cm^{-2}	521	367	296
η (mV) @ j = 10 mA cm^{-2}	710	544	482
η (mV) @ j = 100 mA cm^{-2}	—	755	654
η *vs.* log j (slope) (mV dec^{-1})	199	197	205

Following, chronopotentiometry experiments (Figure 4A) were conducted using 20 wt.-% **$Mn_{19}Br$**/CP electrodes and employing a common procedure,[14] involving a Nafion film to cover the electrode surface. The Nafion polymer generally acts as proton shuttle, transferring protons that are generated during the PCET steps from the electrode surface to the bulk. A similar process occurs in PS-II within the surrounding protein environment of the OEC and results in proton transport through the thylakoid membrane into the lumen (Figure 1A).[57] We decided to use 20 wt% blends as these provide a good compromise between OER performance and quantity of **$Mn_{19}Br$** required in each experiment (*ca.* 10 mg for each experiment). The good mechanical stability of the 20 wt% **$Mn_{19}Br$**/CP electrodes further allows for detailed characterizations over extended periods of time. Throughout the chronopotentiometry experiment using **$Mn_{19}Br$**/CP electrodes at 1 mA cm^{-2}, the overpotential remained stable below 400 mV for a period of over 7 hrs. This chronopotentiometric response is consistent with the LSV measurements. After this time, the catalytic activity gradually decreases suggesting partial catalyst deactivation generating inactive species. Control experiments were conducted to identify other, potentially active species in solution that could derive from $Mn^{II/III}$ leaching over the course of the experiment. For that purpose, CV experiments of the buffer solutions before and after the bulk electrolysis were carried out using unmodified CP electrodes. The recorded voltammograms (Figure 4B) are

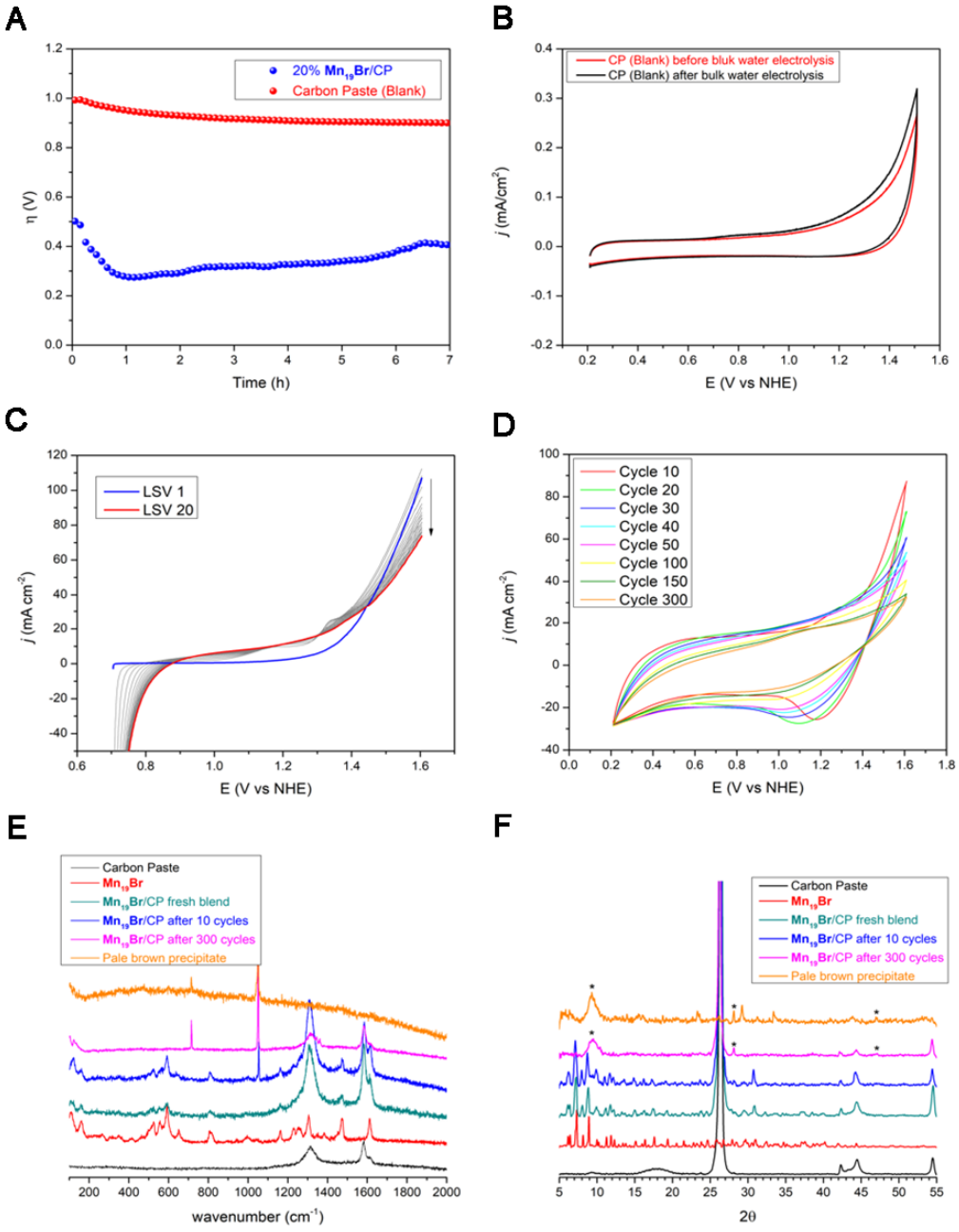

Figure 4. Characterization and stability of the catalyst. (**A**) Chronopotentiometry data of a 20 wt.-% **$Mn_{19}Br$**/CP blend working electrode (blue) and of a carbon-paste-only electrode in the absence of catalyst (red) at a constant current density of 1 mA cm^{-2} in an aqueous phosphate buffer at pH 7.2 using KNO_3 (1 M) as electrolyte. (**B**) Cyclic voltammetry of a carbon-paste-only electrode performed in the same phosphate buffer solution before (red) and after (black) the chronopotentiometry experiment. (**C**) Repetitive linear sweep voltammetry showing the catalyst deactivation; the 1st (blue) and the 20th (red) scan are highlighted. (**D**) Evolution of the cyclic voltammograms over 300 cycles employing a 20 wt.-% **$Mn_{19}Br$**/CP blend working electrode. (**E**) Comparison of the Raman spectrum of **$Mn_{19}Br$** with those of **$Mn_{19}Br$**/CP blends, obtained at different stages of the cyclic voltammetry experiment. The data clearly demonstrates that activity correlates with the quantity of **$Mn_{19}Br$** which is the main component within the blends after 10 CV cycles (blue), whereas no other species can be identified within the system. (**F**) Acquired powder XRD patterns of **$Mn_{19}Br$** and **$Mn_{19}Br$**/CP blends. Asterisks indicate signals arising from the zero-background sample holder (see also Figure S7).

identical, revealing no signs of OER activity. Thus, the presence of catalytically active species in the buffer solution prior, during or after bulk water electrolysis, can strictly be ruled out.

Identification of $Mn_{19}Br$ as the True Catalyst. The outlined experiments clearly demonstrate that **$Mn_{19}Br$**/CP electrodes facilitate electrocatalytic water oxidation at low

onset overpotentials and promote high current densities at moderate overpotentials exceeding most of those reported by other OER catalysts at neutral pH. However, possible Mn cluster transformations and the fate of the catalytically active species were not elucidated by these activity assessments. To unambiguously characterize the Mn catalyst under working conditions, a combination of electrochemical and post-catalytic analyses was conducted. It is important to remark that for those experiments, the stabilizing Nafion membrane was not employed in order to force catalyst decomposition and allowing unequivocal characterization of the composite. The assignment of **Mn_{19}Br** as a genuine molecular OER catalyst was initially substantiated by repeated LSV using 20 wt.-% **Mn_{19}Br**/CP electrodes to follow the kinetics of the catalytic reaction throughout consecutive repetitions (Figure 4C). Tafel plots were constructed from LSV data to evaluate the kinetics and time-dependency of the catalytic activity. As highlighted in Figure 3D, the **Mn_{19}Br**/CP electrode initially shows a slope of 197 mV dec^{-1}, which is characteristic for a diffusion-limited catalytic OER process. After 20 LSV repetitions, however, the slope has increased to 507 mV dec^{-1} indicating the appearance of a catalytically inactive species.

Repetitive CV experiments were carried out to follow possible transformations in the **Mn_{19}Br**/CP electrodes (Figure 4D). Hence, the **Mn_{19}Br**/CP blends were characterized at different stages over 300 cycles. Raman spectra of pristine **Mn_{19}Br** samples were compared to those of *ex-situ* collected **Mn_{19}Br**/CP blends (Figure 4E). The study involved the analysis of **Mn_{19}Br**/CP blends before electrocatalytic tests, after 10 cycles during which maximum current densities are observed and following complete deactivation at 300 cycles. In addition, a pale brown precipitate (**pbp**) that formed on the electrode surface after the conclusion of the experiment was also analyzed. It is well-established that Raman spectroscopy is a highly sensitive surface technique useful for the identification of trace species or intermediates formed under turnover conditions.[58] Figure 4E shows that after 10 cycles, **Mn_{19}Br** constitutes the main compound present in the blend, however, a new band at 1054 cm^{-1} clearly identifies an emerging new species. This latter species, which is assignable to **pbp** that appears on the electrode surface, becomes singular in the spectrum of the de-activated blends collected after 300 cycles. The Raman spectra of **pbp** exclusively feature bands that originate from carbonate vibrations (715 and 1054 cm^{-1}) whereas typical vibrations from MnO_x species are not observed.[59] Thus, these Raman spectroscopy experiments demonstrate that electrocatalytic activity correlates directly to the presence and quantity of **Mn_{19}Br** whereby no traces of other active species are identifiable. This data is further supported by the X-ray powder diffraction patterns (XRD) obtained at the corresponding stages of the reaction (Figure 4F). XRD patterns of pristine **Mn_{19}Br**/CP blends and blends collected after 10 cycles show identical signals that solely derive from **Mn_{19}Br** and the CP matrix. The XRD patterns of blends recovered after 300 cycles and of **pbp** reveal no resemblance to **Mn_{19}Br**-derived patterns. Thus, the XRD patterns also support the singular presence of **Mn_{19}Br** when

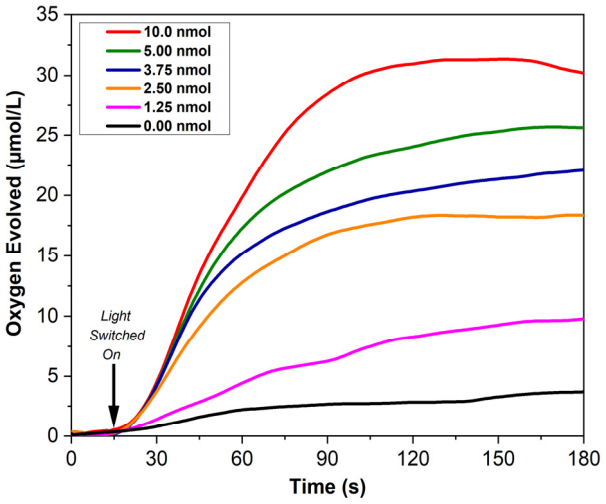

Figure 5. Light-Induced OER Catalysis. Oxygen evolution profiles recorded using a Clark oxygen sensor at different **Mn_{19}Br** loadings; Sample dispersed in an aqueous phosphate buffer at pH 7.0 containing $[Ru(bpy)_2(deeb)](PF_6)_2$ as photosensitizer, and $Na_2S_2O_8$ as sacrificial electron acceptor.

the OER prevails, whilst decomposition products that could give rise to OER activity could not be detected. Additionally, XPS data of pristine **Mn_{19}Br** was compared to that of the **Mn_{19}Br**/CP blend after 10 cycles (Figure S6). Generally, the profile of the $Mn2p_{3/2}$ XPS signal is strongly influenced by minor changes in the coordination environment of the Mn^{II} ions.[60] Comparison of the $Mn2p_{3/2}$ lines of as-prepared **Mn_{19}Br** with those of post-catalytic **Mn_{19}Br**/CP blends show identical features which reveal minor energy shifts from 641.3, 642.8 and 645.4 eV to 641.8, 643.6 and 646.0 eV, respectively. These deconvoluted signals derive from Mn^{II} and Mn^{III} centres, respectively. The latter is a Mn^{II}-derived shake-up satellite peak.[61] The small signal variation to higher energies is characteristic of subtle structural modifications that can result from the partial oxidation of the organic ligands. The assignment is also consistent with the features of the O1s XPS spectra. The signal at 533.1 eV in the spectrum of freshly prepared **Mn_{19}Br** corresponds to the aliphatic alcohol and phenol moieties of the $(HL^{Me})^{2-}$ ligands, whereas in the spectrum of recovered **Mn_{19}Br**/CP blends, two peaks appear at 532.3 and 533.9 eV. An explicit assignment of the latter signals is not trivial as structurally closely related species can give rise to similar binding energies. Hence, the two signals may derive from two distinctive coordinative oxygen atoms of carboxylate functionalities that form upon oxidation of the primary aliphatic alcohol. Alternatively, the peak at 532.3 eV can be assigned to a carbonyl moiety that stems from the partial oxidation of the aliphatic alcohol, whereas the signal at 533.9 eV derives from the phenolic O-donor atom. In both likely scenarios, partial oxidation of the primary alcohol is postulated to be the main pathway of catalyst deactivation. It is noteworthy that XPS signals corresponding to carbonate decomposition product (*ca.* 535.0 eV) were not detected after 10 electrochemical cycles and under

conditions of highest catalytic activity. Moreover, the peaks observed at 531.1 and 530.9 eV, in the spectra of pristine and recovered **$Mn_{19}Br$**, respectively, can directly be assigned to the coordination cluster. All conducted analytical experiments are consistent and confirm that **$Mn_{19}Br$**, or a species whose structure is very close to the cluster core of **$Mn_{19}Br$**, is a genuine OER electrocatalyst that outperforms any other molecular, earth-abundant active OER material working under heterogeneous conditions and at pH = 7 reported to date in terms of catalytic activity.

The morphology and composition of **pbp** were consequently investigated by scanning electron microscopy (SEM) and energy dispersive X-ray spectroscopy (EDX). The material is composed of a 1:1:1 Mn:K:P atomic ratio and elemental mapping confirms a homogeneous elemental dispersion throughout the solid (Figure S8). A detailed FT-IR analysis identifies this inactive amorphous precipitate as manganese-potassium carbonate-phosphate (Figure S9).[62] The bands at 540, 574, and 616 cm^{-1} can be assigned to the δ_v valence vibrations of the PO_4^{3-} group, whilst symmetric ν_1 vibrations reveal bands between 780 and 995 cm^{-1}, whereas the ν_3 asymmetric vibrations result in signals between 1034 and 1225 cm^{-1}. The ν_3 deformation vibrations of the CO_3^{2-} group give rise to a band at 1376 cm^{-1}. The signal at 1634 cm^{-1} derives from the OH^- deformation vibrations of water molecules which further result in a band at 474 cm^{-1}. It is evident that the inorganic carbonate ions derive from the 2,6-bis(hydroxymethyl)-*p*-cresol ligand and their presence confirms the prevailing decomposition pathway of **$Mn_{19}Br$**. Thus, potential future structural modifications of **$Mn_{19}Br$** should involve the modification of the H_3L^{Me} ligand to achieve robust cresol derivatives to increase the catalyst stability under the harsh oxidative conditions.

Light-Induced OER Catalysis. The intrinsic OER characteristics of the **$Mn_{19}Br$** system at neutral pH conditions are advantageous for the development of photoanodes within artificial photosynthetic cells.[13] To this end, **$Mn_{19}Br$** is required to perform photocatalytically in combination with light absorbers on electrode surfaces. Therefore, it was important to substantiate the catalytic performance of **$Mn_{19}Br$** under light-driven OER conditions. A well-established literature protocol,[63] involving a three-component system consisting of a colloidal suspension of **$Mn_{19}Br$**, $[Ru(bpy)_2(deeb)](PF_6)_2$ as photosensitizer and $Na_2S_2O_8$ as sacrificial electron acceptor was applied. Further, control experiments in which one of each of the three photocatalytic components were removed resulted in negligible O_2 evolution, demonstrating that all three components are integral for overall OER activity (Table S2). Moreover, when equivalent quantities of the 2,6-bis(hydroxymethyl)-*p*-cresol ligand (H_3L^{Me}) or $MnBr_2{\cdot}4H_2O$ were used instead of **$Mn_{19}Br$**, demonstrate that the observed activity does not arise from the ligand, impurities, Mn^{II} ions leaching, or *in-situ* MnO_x formation (Figure S10).

The O_2 evolution activity of **$Mn_{19}Br$** in an aqueous, deaerated phosphate-buffered solution was confirmed and monitored in real-time using a Clark electrode. Upon light-irradiation (LED lamp, λ = 470 nm), nanomolar catalyst loadings (1.25 nmol – 10.00 nmol) give rise to high activity, whereby the dissolved O_2 quantity continuously rises for *ca.* 120 seconds, before reaching a plateau (Figure 5). Net O_2 production increases with the catalyst concentration following pseudo first-order kinetics, which is indicative of O-O bond formation *via* nucleophilic attack by H_2O molecules. Maximum O_2 liberation of 160 nmol was achieved at a catalyst loading of 10.00 nmol, with a corresponding TON = 16. Decreasing the loading of **$Mn_{19}Br$** further coincided with increasing TONs, *e.g.* a TON = 40 was achieved at a catalyst loading of 1.25 nmol. Following the cessation of O_2 evolution by **$Mn_{19}Br$**, the catalyst was recycled by adding fresh quantities of photosensitizer and sacrificial oxidant to the reaction vial and repeating the experiment (Figure S11). Although the activity decreased with each subsequent photocatalytic test probably due to a combination of catalyst deactivation, its insolubility and increase of the ionic strength of the solution, a total TON = 55 was achieved over 25 minutes.

The highest turnover frequency (TOF) of 0.72 s^{-1} was observed at a catalyst loading of 2.50 nmol within the first 10s of the reaction (see Table 2). This is several times higher than the TOFs of any previously reported MnO_x species, and the highest of any other molecular, heterogeneously operating Mn coordination cluster under neutral pH conditions;[64] hence the data is supportive of the electrochemical studies. However, it is worth noting that the determined TONs and TOFs do not fully represent the activity of the complex, considering that **$Mn_{19}Br$** is insoluble in aqueous systems and only a minor number of Mn sites are readily available to promote the water oxidation reaction. Therefore, calculated TONs are underestimated, and higher values would be expected using soluble cluster derivatives in molecular solutions in which all the catalytically active metallic centers are readily accessible for H_2O molecules.

Post-catalytic **$Mn_{19}Br$** isolation and characterization are difficult tasks due to the low quantities of catalyst employed in these experiments. Hence, Raman spectroscopy experiments of the dried residues of the photocatalytic three-component mixture were performed before and after irradiation (Figure S12). As expected, **$Mn_{19}Br$**-derived signals disappear during the experiments indicating catalyst decomposition. Significantly, signals between 200 – 750 cm^{-1} that may arise from the *in-situ* formation of OER-active MnO_x species could not be detected in the spectrum of the post-irradiated catalytic mixture. Hence, as MnO_x compounds are typically highly Raman active in this region and OER active, the experiments rule out the formation of MnO_x under the working conditions of the photocatalytic O_2 evolution.[65,66]

Table 2. Turnover number (TON) and turnover frequencies (TOF) for light-induced OER catalysis experiments. Data obtained at various $Mn_{19}Br$ catalyst loadings.

Catalyst Loading (nmol)	TON	TOF (s^{-1})
10.00	16	0.33
5.00	26	0.53
3.75	30	0.64
2.50	36	0.72
1.25	40	0.48

DISCUSSION AND CONCLUSION

In summary, we report a bio-inspired, high-nuclearity Mn-oxo cluster (**$Mn_{19}Br$**) composed of cubane motifs that yields high catalytic OER activity in the solid state. As a part of modified carbon paste electrodes, **$Mn_{19}Br$** gives rise to a very low onset potential for the catalytic oxidation of water at η = 255 mV. Additionally, high current densities of 100 mA cm^{-2} are delivered at η = 654 mV. In combination with a proton-conducting Nafion membrane-layer, the OER catalyst delivers a current density of 1 mA cm^{-2} for over 7 hrs at an overpotential below 400 mV. This overpotential can be reduced by increasing the quantity of **$Mn_{19}Br$** in the carbon blend, as demonstrated by linear sweep voltammetry experiments. Under light-induced water oxidation conditions, TONs and TOFs of 40 and 0.72 s^{-1} were calculated. A thorough characterization protocol of the modified **$Mn_{19}Br$**/CP electrodes allowed us to unambiguously identify the fate of the catalytically active species.

The observed OER activity directly correlates with the quantity of **$Mn_{19}Br$** and clearly results from a synergistic effect of a bio-inspired Mn-oxo cluster and the stabilizing redox-active organic ligands that interact with a conductive stabilizing carbon-based matrix. The Nafion membrane efficiently removes the produced protons from the electrode surface and protects the catalyst for prolonged periods of time. Hence, the system replicates key features of OEC environment in PS-II. It is important to note that the present study was carried out at neutral pH values, at 1 atm, and room temperature, where **$Mn_{19}Br$**/CP electrodes have shown good OER performance that is desired for the development of artificial photosynthetic cells for direct solar-to-fuel applications. To date, the most attractive, noble metal free material operating under neutral pH conditions is a cobalt oxide-phosphate catalyst (Co-P_i) as established by the seminal work by Nocera and co-workers more than one decade ago.[19] Deposited on the surface of an indium tin oxide (ITO) electrode, Co-P_i (and its Co-B_i derivative) catalyzes water oxidation delivering 1 mA cm^{-2} at an applied overpotential of 410 mV at pH = 7 whereas higher current densities of 100 mA cm^{-2}_{geom} could only be achieved using high-surface area electrodes such as Ni foams and carrying out the experiment in a flow-through electrochemical cell at pH 9.2.[67] Such experimental difficulties in providing high charge-carrier mobilities at moderate overpotentials, underline the activity characteristics of the **$Mn_{19}Br$** composite system. The observed catalytic activity of the **$Mn_{19}Br$** system derives from the polynuclear core structure of the oxo-cluster which contains 'dangling' Mn^{II} centers that can interact with water substrates and which can accumulate charge equivalents along the different metallic centers, hence facilitating multiple-electron redox processes. The latter characteristic is one of the most important features of natural enzymes to facilitate rapid multiple electron/cascade transformations[68] and is well-established for molecular oxo-clusters, including polyoxometalates.[69–72] Equally important for the reactivity of **$Mn_{19}Br$**, within the electrochemical setup, is the oxidizable *p*-cresol $(HL^{Me})^{2-}$ ligand derivative that promotes the electron transport between the Mn cluster core and the stabilizing carbon matrix, thus providing analogies to the natural tyrosine-Y161 or plastoquinone functionalities within the D1 unit of PS-II. The outlined concept establishes a synthetic avenue to highly active catalysts using abundant, non-toxic metal ions which will be applicable to other cluster compounds and diverse redox-active ligands. The latter can synthetically be modified to increase the stability of the catalytic systems whilst computational modelling might elucidate mechanistic analogies or differences between **$Mn_{19}Br$** and the OEC.

ASSOCIATED CONTENT

The Supporting Information is available free of charge on the ACS Publication website. Materials, Methods, Figures S1–S12, Tables S1 and S2.

AUTHOR INFORMATION

Corresponding Author

*schmittw@tcd.ie
*sorianoj@tcd.ie

Present Addresses

† Reliance Industries Limited, Mumba
§ LBIC - London Brunel International College, London, UK

Author Contributions

W.S. conceived the project; J.S-L. carried out the electrochemical studies, analyses & characterizations; R.E. carried out photocatalytic studies, compound analyses & characterizations; A.C.K. carried out photocatalytic studies, analyses & X-ray crystallography; A.M.A. and M.M. synthesized and characterized the compound. W.S., J.S-L. and R.E. prepared the

manuscript; all authors contributed to discussions throughout the project and the final editing of the manuscript.

Notes

Authors declare no competing interests

ACKNOWLEDGMENT

J.S-L. acknowledges the funding from the European Union's Horizon 2020 research and innovation programme under the Marie Skłodowska-Curie grant agreement No 713567. This research was funded by Science Foundation Ireland (13/IA/1896) and the European Research Council (CoG 2014–647719).

REFERENCES AND NOTES

(1) Hoffert, M. I.; Caldeira, K.; Jain, A. K.; Haites, E. F.; Harvey, L. D. D.; Potter, S. D.; Schlesinger, M. E.; Schneider, S. H.; Watts, R. G.; Wigley, T. M. L.; Wuebbles, D. J. Energy Implications of Future Stabilization of Atmospheric CO_2 Content. *Nature* **1998**, *395*, 881–884, DOI 10.1038/27638.

(2) Lewis, N. S.; Nocera, D. G. Powering the Planet: Chemical Challenges in Solar Energy Utilization. *Proc. Natl. Acad. Sci.* **2006**, *103*, 15729–15735, DOI 10.1073/pnas.0603395103.

(3) Steffen, W.; Richardson, K.; Rockstrom, J.; Cornell, S. E.; Fetzer, I.; Bennett, E. M.; Biggs, R.; Carpenter, S. R.; de Vries, W.; de Wit, C. A.; Folke, C.; Gerten, D.; Heinke, J.; Mace, G. M.; Persson, L. M.; Ramanathan, V.; Reyers, B.; Sorlin, S. Planetary Boundaries: Guiding Human Development on a Changing Planet. *Science* **2015**, *347*, 1259855–1259855, DOI 10.1126/science.1259855.

(4) McKone, J. R.; Lewis, N. S.; Gray, H. B. Will Solar-Driven Water-Splitting Devices See the Light of Day? *Chem. Mater.* **2014**, *26*, 407–414, DOI 10.1021/cm4021518.

(5) McCrory, C. C. L.; Jung, S.; Ferrer, I. M.; Chatman, S. M.; Peters, J. C.; Jaramillo, T. F. Benchmarking Hydrogen Evolving Reaction and Oxygen Evolving Reaction Electrocatalysts for Solar Water Splitting Devices. *J. Am. Chem. Soc.* **2015**, *137*, 4347–4357, DOI 10.1021/ja510442p.

(6) Lyons, M. E. G.; Doyle, R. L.; Browne, M. P.; Godwin, I. J.; Rovetta, A. A. S. Recent Developments in Electrochemical Water Oxidation. *Curr. Opin. Electrochem.* **2017**, *1*, 40–45, DOI 10.1016/j.coelec.2016.12.005.

(7) Soriano-López, J.; Schmitt, W.; García-Melchor, M. Computational Modelling of Water Oxidation Catalysts. *Curr. Opin. Electrochem.* **2018**, *7*, 22–30, DOI 10.1016/j.coelec.2017.10.001.

(8) Dau, H.; Zaharieva, I. Principles, Efficiency, and Blueprint Character of Solar-Energy Conversion in Photosynthetic Water Oxidation. *Acc. Chem. Res.* **2009**, *42*, 1861–1870, DOI 10.1021/ar900225y.

(9) Kiwi, J.; Grätzel, M. Colloidal Redox Catalysts for Evolution of Oxygen and for Light-Induced Evolution of Hydrogen from Water. *Angew. Chemie Int. Ed. English* **1979**, *18*, 624–626, DOI 10.1002/anie.197906241.

(10) Seitz, L. C.; Dickens, C. F.; Nishio, K.; Hikita, Y.; Montoya, J.; Doyle, A.; Kirk, C.; Vojvodic, A.; Hwang, H. Y.; Norskov, J. K.; Jaramillo, T. F. A Highly Active and Stable IrO_x/$SrIrO_3$catalyst for the Oxygen Evolution Reaction. *Science* **2016**, *353*, 1011–1014, DOI 10.1126/science.aaf5050.

(11) Blakemore, J. D.; Crabtree, R. H.; Brudvig, G. W. Molecular Catalysts for Water Oxidation. *Chem. Rev.* **2015**, *115*, 12974–13005, DOI 10.1021/acs.chemrev.5b00122.

(12) Galán-Mascarós, J. R. Water Oxidation at Electrodes Modified with Earth-Abundant Transition-Metal Catalysts. *ChemElectroChem* **2015**, *2*, 37–50, DOI 10.1002/celc.201402268.

(13) Roger, I.; Shipman, M. A.; Symes, M. D. Earth-Abundant Catalysts for Electrochemical and Photoelectrochemical Water Splitting. *Nat. Rev. Chem.* **2017**, *1*, 0003, DOI 10.1038/s41570-016-0003.

(14) Blasco-Ahicart, M.; Soriano-López, J.; Carbó, J. J.; Poblet, J. M.; Galan-Mascaros, J. R. Polyoxometalate Electrocatalysts Based on Earth-Abundant Metals for Efficient Water Oxidation in Acidic Media. *Nat. Chem.* **2018**, *10*, 24–30, DOI 10.1038/nchem.2874.

(15) Fisher, K. J.; Materna, K. L.; Mercado, B. Q.; Crabtree, R. H.; Brudvig, G. W. Electrocatalytic Water Oxidation by a Copper(II) Complex of an Oxidation-Resistant Ligand. *ACS Catal.* **2017**, *7*, 3384–3387, DOI 10.1021/acscatal.7b00494.

(16) Lloret-Fillol, J.; Codolà, Z.; Garcia-Bosch, I.; Gómez, L.; Pla, J. J.; Costas, M. Efficient Water Oxidation Catalysts Based on Readily Available Iron Coordination Complexes. *Nat. Chem.* **2011**, *3*, 807–813, DOI 10.1038/nchem.1140.

(17) Schwarz, B.; Forster, J.; Anjass, M. H.; Daboss, S.; Kranz, C.; Streb, C. From Molecular to Colloidal Manganese Vanadium Oxides for Water Oxidation Catalysis. *Chem. Commun.* **2017**, *53*, 11576–11579, DOI 10.1039/C7CC06840A.

(18) Gerken, J. B.; McAlpin, J. G.; Chen, J. Y. C.; Rigsby, M. L.; Casey, W. H.; Britt, R. D.; Stahl, S. S. Electrochemical Water Oxidation with Cobalt-Based Electrocatalysts from pH 0–14: The Thermodynamic Basis for Catalyst Structure, Stability, and Activity. *J. Am. Chem. Soc.* **2011**, *133*, 14431–14442, DOI 10.1021/ja205647m.

(19) Kanan, M. W.; Nocera, D. G. In Situ Formation of an Oxygen-Evolving Catalyst in Neutral Water Containing Phosphate and Co^{2+}. *Science* **2008**, *321*, 1072–1075, DOI 10.1126/science.1162018.

(20) Zhang, B.; Zheng, X.; Voznyy, O.; Comin, R.; Bajdich, M.; Garcia-Melchor, M.; Han, L.; Xu, J.; Liu, M.; Zheng, L.; Garcia de Arquer, F. P.; Dinh, C. T.; Fan, F.; Yuan, M.; Yassitepe, E.; Chen, N.; Regier, T.; Liu, P.; Li, Y.; De Luna, P.; Janmohamed, A.; Xin, H. L.; Yang, H.; Vojvodic, A.; Sargent, E. H. Homogeneously Dispersed Multimetal Oxygen-Evolving Catalysts. *Science* **2016**, *352*, 333–337, DOI 10.1126/science.aaf1525.

(21) Ng, J. W. D.; García-Melchor, M.; Bajdich, M.; Chakthranont, P.; Kirk, C.; Vojvodic, A.; Jaramillo, T. F. Gold-Supported Cerium-Doped NiO_x Catalysts for Water Oxidation. *Nat. Energy* **2016**, *1*, 16053, DOI 10.1038/nenergy.2016.53.

(22) Carmo, M.; Fritz, D. L.; Mergel, J.; Stolten, D. A Comprehensive Review on PEM Water Electrolysis. *Int. J. Hydrogen Energy* **2013**, *38*, 4901–4934, DOI 10.1016/j.ijhydene.2013.01.151.

(23) Styring, S. Artificial Photosynthesis for Solar Fuels. *Faraday Discuss.* **2012**, *155*, 357–376, DOI 10.1039/C1FD00113B.

(24) Tachibana, Y.; Vayssieres, L.; Durrant, J. R. Artificial Photosynthesis for Solar Water-Splitting. *Nat. Photonics* **2012**, *6*, 511–518, DOI 10.1038/nphoton.2012.175.

(25) BENNETT, J. Electrodes for Generation of Hydrogen and Oxygen from Seawater. *Int. J. Hydrogen Energy* **1980**, *5*, 401–408, DOI 10.1016/0360-3199(80)90021-X.

(26) Yan, L.; Zhang, B.; Zhu, J.; Liu, Z.; Zhang, H.; Li, Y. Callistemon-like Zn and S Codoped CoP Nanorod Clusters as Highly Efficient Electrocatalysts for Neutral-pH Overall Water Splitting. *J. Mater. Chem. A* **2019**, *7*, 22453–22462, DOI 10.1039/C9TA08812A.

(27) Cheng, P.; Yuan, C.; Zhou, Q.; Hu, X.; Li, J.; Lin, X.; Wang, X.; Jin, M.; Shui, L.; Gao, X.; Nötzel, R.; Zhou, G.; Zhang, Z.; Liu, J. Core–Shell MoS_2@CoO Electrocatalyst for Water Splitting in Neural and Alkaline Solutions. *J. Phys. Chem. C* **2019**, *123*, 5833–5839, DOI 10.1021/acs.jpcc.8b10954.

(28) Cho, K. H.; Seo, H.; Park, S.; Lee, Y. H.; Lee, M. Y.; Cho, N. H.; Nam, K. T. Uniform, Assembled 4 nm Mn_3O_4 Nanoparticles as Efficient Water Oxidation Electrocatalysts at Neutral pH. *Adv. Funct. Mater.* **2020**, *30*, 1910424, DOI 10.1002/adfm.201910424.

(29) Jin, K.; Chu, A.; Park, J.; Jeong, D.; Jerng, S. E.; Sim, U.; Jeong, H.-Y.; Lee, C. W.; Park, Y.-S.; Yang, K. D.; Kumar Pradhan,

G.; Kim, D.; Sung, N.-E.; Hee Kim, S.; Nam, K. T. Partially Oxidized Sub-10 nm MnO Nanocrystals with High Activity for Water Oxidation Catalysis. *Sci. Rep.* **2015**, *5*, 10279, DOI 10.1038/srep10279.

(30) Zhang, B.; Chen, H.; Daniel, Q.; Philippe, B.; Yu, F.; Valvo, M.; Li, Y.; Ambre, R. B.; Zhang, P.; Li, F.; Rensmo, H.; Sun, L. Defective and " c -Disordered" Hortensia -like Layered MnO_x as an Efficient Electrocatalyst for Water Oxidation at Neutral pH. *ACS Catal.* **2017**, *7*, 6311–6322, DOI 10.1021/acscatal.7b00420.

(31) Cook, T. R.; Dogutan, D. K.; Reece, S. Y.; Surendranath, Y.; Teets, T. S.; Nocera, D. G. Solar Energy Supply and Storage for the Legacy and Non Legacy Worlds. *Chem. Rev.* **2010**, *110*, 6474–6502, DOI 10.1021/cr100246c.

(32) Montoya, J. H.; Seitz, L. C.; Chakthranont, P.; Vojvodic, A.; Jaramillo, T. F.; Nørskov, J. K. Materials for Solar Fuels and Chemicals. *Nat. Mater.* **2017**, *16*, 70–81, DOI 10.1038/nmat4778.

(33) Seh, Z. W.; Kibsgaard, J.; Dickens, C. F.; Chorkendorff, I.; Nørskov, J. K.; Jaramillo, T. F. Combining Theory and Experiment in Electrocatalysis: Insights into Materials Design. *Science* **2017**, 355, eaad4998, DOI 10.1126/science.aad4998.

(34) Walter, M. G.; Warren, E. L.; McKone, J. R.; Boettcher, S. W.; Mi, Q.; Santori, E. A.; Lewis, N. S. Solar Water Splitting Cells. *Chem. Rev.* **2010**, *110*, 6446–6473, DOI 10.1021/cr1002326.

(35) Seitz, L. C.; Chen, Z.; Forman, A. J.; Pinaud, B. A.; Benck, J. D.; Jaramillo, T. F. Modeling Practical Performance Limits of Photoelectrochemical Water Splitting Based on the Current State of Materials Research. *ChemSusChem* **2014**, *7*, 1372–1385, DOI 10.1002/cssc.201301030.

(36) Haumann, M. Photosynthetic O_2 Formation Tracked by Time-Resolved X-Ray Experiments. *Science* **2005**, *310*, 1019–1021, DOI 10.1126/science.1117551.

(37) Siegbahn, P. E. M. Nucleophilic Water Attack Is Not a Possible Mechanism for O–O Bond Formation in Photosystem II. *Proc. Natl. Acad. Sci.* **2017**, *114*, 4966–4968, DOI 10.1073/pnas.1617843114.

(38) Nocera, D. G. The Artificial Leaf. *Acc. Chem. Res.* **2012**, *45*, 767–776, DOI 10.1021/ar2003013.

(39) Haxel, G. B.; Hedrick, J. B.; Orris, G. J.; Stauffer, P. H.; Hendley II, J. W. *Rare Earth Elements: Critical Resources for High Technology*; 2002, DOI 10.3133/fs08702.

(40) Hocking, R. K.; Brimblecombe, R.; Chang, L. Y.; Singh, A.; Cheah, M. H.; Glover, C.; Casey, W. H.; Spiccia, L. Water-Oxidation Catalysis by Manganese in a Geochemical-like Cycle. *Nat. Chem.* **2011**, *3*, 461–466, DOI 10.1038/nchem.1049.

(41) Goberna-Ferrón, S.; Soriano-López, J.; Galán-Mascarós, J. Activity and Stability of the Tetramanganese Polyanion $[Mn_4(H_2O)_2(PW_9O_{34})_2]^{10-}$ during Electrocatalytic Water Oxidation. *Inorganics* **2015**, *3*, 332–340, DOI 10.3390/inorganics3030332.

(42) Brimblecombe, R.; Swiegers, G. F.; Dismukes, G. C.; Spiccia, L. Sustained Water Oxidation Photocatalysis by a Bioinspired Manganese Cluster. *Angew. Chemie Int. Ed.* **2008**, *47*, 7335–7338, DOI 10.1002/anie.200801132.

(43) Al-Oweini, R.; Sartorel, A.; Bassil, B. S.; Natali, M.; Berardi, S.; Scandola, F.; Kortz, U.; Bonchio, M. Photocatalytic Water Oxidation by a Mixed-Valent $Mn^{III}_3Mn^{IV}O_3$ Manganese Oxo Core That Mimics the Natural Oxygen-Evolving Center. *Angew. Chemie Int. Ed.* **2014**, *53*, 11182–11185, DOI 10.1002/anie.201404664.

(44) Yan, Y.; Lee, J. S.; Ruddy, D. A. Structure–Function Relationships for Electrocatalytic Water Oxidation by Molecular $[Mn_{12}O_{12}]$ Clusters. *Inorg. Chem.* **2015**, *54*, 4550–4555, DOI 10.1021/acs.inorgchem.5b00398.

(45) Maayan, G.; Gluz, N.; Christou, G. A Bioinspired Soluble Manganese Cluster as a Water Oxidation Electrocatalyst with Low Overpotential. *Nat. Catal.* **2018**, *1*, 48–54, DOI 10.1038/s41929-017-0004-2.

(46) Ghosh, T.; Maayan, G. Efficient Homogeneous Electrocatalytic Water Oxidation by a Manganese Cluster with an Overpotential of Only 74 mV. *Angew. Chemie Int. Ed.* **2019**, *58*, 2785–2790, DOI 10.1002/anie.201813895.

(47) Baranov, S. V.; Ananyev, G. M.; Klimov, V. V.; Dismukes, G. C. Bicarbonate Accelerates Assembly of the Inorganic Core of the Water-Oxidizing Complex in Manganese-Depleted Photosystem II: A Proposed Biogeochemical Role for Atmospheric Carbon Dioxide in Oxygenic Photosynthesis †. *Biochemistry* **2000**, *39*, 6060–6065, DOI 10.1021/bi992682c.

(48) Vogt, L.; Vinyard, D. J.; Khan, S.; Brudvig, G. W. Oxygen-Evolving Complex of Photosystem II: An Analysis of Second-Shell Residues and Hydrogen-Bonding Networks. *Curr. Opin. Chem. Biol.* **2015**, *25*, 152–158, DOI 10.1016/j.cbpa.2014.12.040.

(49) Ako, A. M.; Hewitt, I. J.; Mereacre, V.; Clérac, R.; Wernsdorfer, W.; Anson, C. E.; Powell, A. K. A Ferromagnetically Coupled Mn_{19} Aggregate with a Record S=83/2 Ground Spin State. *Angew. Chemie Int. Ed.* **2006**, *45*, 4926–4929, DOI 10.1002/anie.200601467.

(50) Ako, A. M.; Lan, Y.; Hampe, O.; Cremades, E.; Ruiz, E.; Anson, C. E.; Powell, A. K. All-Round Robustness of the Mn_{19} Coordination Cluster System: Experimental Validation of a Theoretical Prediction. *Chem. Commun.* **2014**, *50*, 5847–5850, DOI 10.1039/C4CC01264J.

(51) Chevallot-Beroux, E.; Ako, A. M.; Schmitt, W.; Twamley, B.; Moran, J.; Corinne, B.; Ruhlmann, L.; Mameri, S. Synthesis of New Mn_{19} Analogues and Their Structural, Electrochemical and Catalytic Properties. *Dalt. Trans.* **2019**, *48*, 4830–4836, DOI 10.1039/c8dt04807j.

(52) Umena, Y.; Kawakami, K.; Shen, J.-R.; Kamiya, N. Crystal Structure of Oxygen-Evolving Photosystem II at a Resolution of 1.9 Å. *Nature* **2011**, *473*, 55–60, DOI 10.1038/nature09913.

(53) Siegbahn, P. E. M.; Blomberg, M. R. A. Important Roles of Tyrosines in Photosystem II and Cytochrome Oxidase. *Biochim. Biophys. Acta - Bioenerg.* **2004**, *1655*, 45–50, DOI 10.1016/j.bbabio.2003.07.003.

(54) Soriano-López, J.; Goberna-Ferrón, S.; Vigara, L.; Carbó, J. J.; Poblet, J. M.; Galán-Mascarós, J. R. Cobalt Polyoxometalates as Heterogeneous Water Oxidation Catalysts. *Inorg. Chem.* **2013**, *52*, 4753–4755, DOI 10.1021/ic4001945.

(55) Weinberg, N. L.; Weinberg, H. R. Electrochemical Oxidation of Organic Compounds. *Chem. Rev.* **1968**, *68*, 449–523, DOI 10.1021/cr60254a003.

(56) Doyle, R. L.; Lyons, M. E. G. The Oxygen Evolution Reaction: Mechanistic Concepts and Catalyst Design. In *Photoelectrochemical Solar Fuel Production: From Basic Principles to Advanced Devices*; Springer International Publishing: Cham, 2016; pp 41–104, DOI 10.1007/978-3-319-29641-8_2.

(57) Ferreira, K. N.; Iverson, T. M.; Maghlaoui, K.; Barber, J.; Iwata, S. Architecture of the Photosynthetic Oxygen-Evolving Center. *Science* **2004**, *303*, 1831–1838, DOI 10.1126/science.1093087.

(58) Ahn, H. S.; Tilley, T. D. Electrocatalytic Water Oxidation at Neutral pH by a Nanostructured $Co(PO_3)_2$ Anode. *Adv. Funct. Mater.* **2013**, *23*, 227–233, DOI 10.1002/adfm.201200920.

(59) Ramírez, A.; Hillebrand, P.; Stellmach, D.; May, M. M.; Bogdanoff, P.; Fiechter, S. Evaluation of MnO_x , Mn_2O_3 and Mn_3O_4 Electrodeposited Films for the Oxygen Evolution Reaction of Water. *J. Phys. Chem. C* **2014**, *118*, 14073–14081, DOI 10.1021/jp500939d.

(60) Ilton, E. S.; Post, J. E.; Heaney, P. J.; Ling, F. T.; Kerisit, S. N. XPS Determination of Mn Oxidation States in Mn (Hydr)Oxides. *Appl. Surf. Sci.* **2016**, *366*, 475–485, DOI 10.1016/j.apsusc.2015.12.159.

(61) Biesinger, M. C.; Payne, B. P.; Grosvenor, A. P.; Lau, L. W. M.; Gerson, A. R.; Smart, R. S. C. Resolving Surface Chemical States in XPS Analysis of First Row Transition Metals, Oxides and Hydroxides: Cr, Mn, Fe, Co and Ni. *Appl. Surf. Sci.* **2011**, *257*, 2717–2730, DOI 10.1016/j.apsusc.2010.10.051.

(62) F. Koroleva, L. L. P. L. N. P. G. Biomaterial Based on Doped Calcium Carbonate-Phosphate for Active Osteogenesis. *J. Biomater. Nanobiotechnol.* **2012**, *03*, 226–237, DOI 10.4236/jbnb.2012.32028.

(63) Abdel-Magied, A. F.; Shatskiy, A.; Liao, R.-Z.; Laine, T. M.; Arafa, W. A. A.; Siegbahn, P. E. M.; Kärkäs, M. D.; Åkermark, B.; Johnston, E. V. Chemical and Photochemical Water Oxidation Mediated by an Efficient Single-Site Ruthenium Catalyst. *ChemSusChem* **2016**, *9*, 3448–3456, DOI 10.1002/cssc.201601171.

(64) Lee, L. Y. S.; Wong, K.-Y. Recent Development in Water Oxidation Catalysts Based on Manganese and Cobalt Complexes. In *Organometallics and Related Molecules for Energy Conversion*; Wang, W.-Y., Ed.; Springer Berlin Heidelberg, 2015; pp 365–394, DOI 10.1007/978-3-662-46054-2_13.

(65) Bernardini, S.; Bellatreccia, F.; Casanova Municchia, A.; Della Ventura, G.; Sodo, A. Raman Spectra of Natural Manganese Oxides. *J. Raman Spectrosc.* **2019**, *50*, 873–888, DOI 10.1002/jrs.5583.

(66) Buciuman, F.; Patcas, F.; Craciun, R.; Zahn, D. R. T. Vibrational Spectroscopy of Bulk and Supported Manganese Oxides. *Phys. Chem. Chem. Phys.* **1999**, *1*, 185–190, DOI 10.1039/a807821a.

(67) Esswein, A. J.; Surendranath, Y.; Reece, S. Y.; Nocera, D. G. Highly Active Cobalt Phosphate and Borate Based Oxygen Evolving Catalysts Operating in Neutral and Natural Waters. *Energy Environ. Sci.* **2011**, *4*, 499–504, DOI 10.1039/CoEE00518E.

(68) McEvoy, J. P.; Brudvig, G. W. Water-Splitting Chemistry of Photosystem II. *Chem. Rev.* **2006**, *106*, 4455–4483, DOI 10.1021/cr0204294.

(69) López, X.; Carbó, J. J.; Bo, C.; Poblet, J. M. Structure, Properties and Reactivity of Polyoxometalates: A Theoretical Perspective. *Chem. Soc. Rev.* **2012**, *41*, 7537, DOI 10.1039/c2cs35168d.

(70) Martin-Sabi, M.; Soriano-López, J.; Winter, R. S.; Chen, J.-J.; Vilà-Nadal, L.; Long, D.-L.; Galán-Mascarós, J. R.; Cronin, L. Redox Tuning the Weakley-Type Polyoxometalate Archetype for the Oxygen Evolution Reaction. *Nat. Catal.* **2018**, *1*, 208–213, DOI 10.1038/s41929-018-0037-1.

(71) Lv, H.; Song, J.; Geletii, Y. V.; Vickers, J. W.; Sumliner, J. M.; Musaev, D. G.; Kögerler, P.; Zhuk, P. F.; Bacsa, J.; Zhu, G.; Hill, C. L. An Exceptionally Fast Homogeneous Carbon-Free Cobalt-Based Water Oxidation Catalyst. *J. Am. Chem. Soc.* **2014**, *136*, 9268–9271, DOI 10.1021/ja5045488.

(72) Goberna-Ferrón, S.; Vigara, L.; Soriano-López, J.; Galán-Mascarós, J. R. Identification of a Nonanuclear $\{Co^{II}_9\}$ Polyoxometalate Cluster as a Homogeneous Catalyst for Water Oxidation. *Inorg. Chem.* **2012**, *51*, 11707–11715, DOI 10.1021/ic301618h.

† The European Commission, under the European Union (EU) Raw Materials Initiative recognizes the availability of manganese and other Earth-abundant elements, whilst the supply of 27 listed critical raw materials is restricted (Commission's Communication 'On the 2017 list of Critical Raw Materials for the EU' (COM(2017)490). Available at: https://eur-lex.europa.eu/legal-content/EN/TXT/?uri=CELEX: 52017DC0490

TOC Graphics:

A bioinspired high-nuclearity manganese-oxo cluster containing multiple cubane motifs and which is stabilized by redox-active aromatic organic ligands shows heterogeneous water oxidation catalytic activity at neutral pH values achieving high current densities.